Measurement of the $B_s^0 \to \mu^+\mu^-$ branching fraction and search for $B^0 \to \mu^+\mu^-$ decays at the LHCb experiment

Additional Material

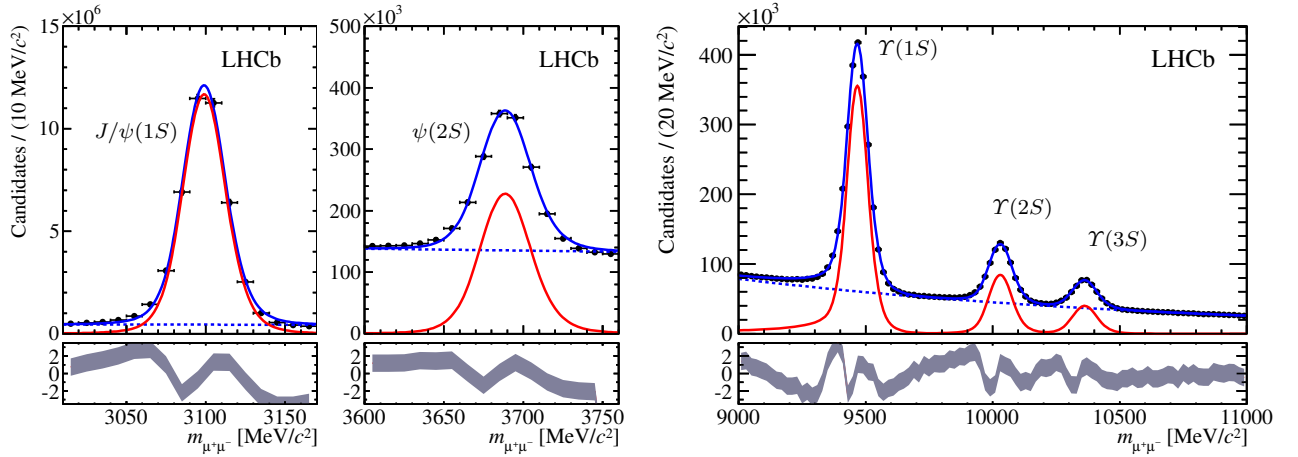Figure 1: Dimuon invariant mass distribution for $J/\psi(1S) \to \mu^+\mu^-$, $\psi(2S) \to \mu^+\mu^-$ and $\Upsilon(1S, 2S, 3S) \to \mu^+\mu^-$ decays in data. A fit to the distribution is superimposed: resonances are described by the sum of two Crystal Ball functions (red line) while the combinatorial background is described by an exponential function (blue dashed line). The full PDF is represented by a continuous blue line.
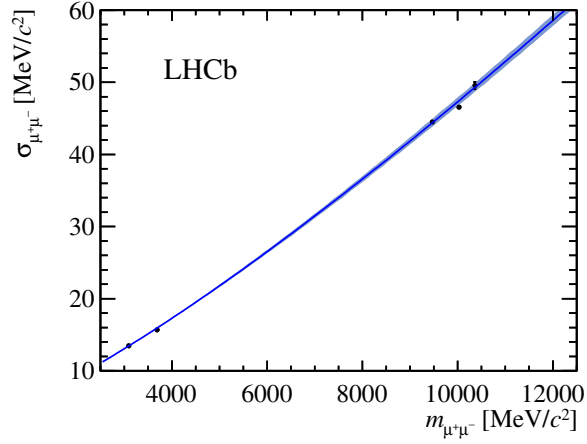
Figure 2: Invariant mass resolution for dimuons obtained from fits to the charmonium and bottomonium resonances (red dots) and a power law function (blue with light blue uncertainty bands) fitted to these data points and used to interpolate to the mass of the B^0 and B_s^0 mesons.
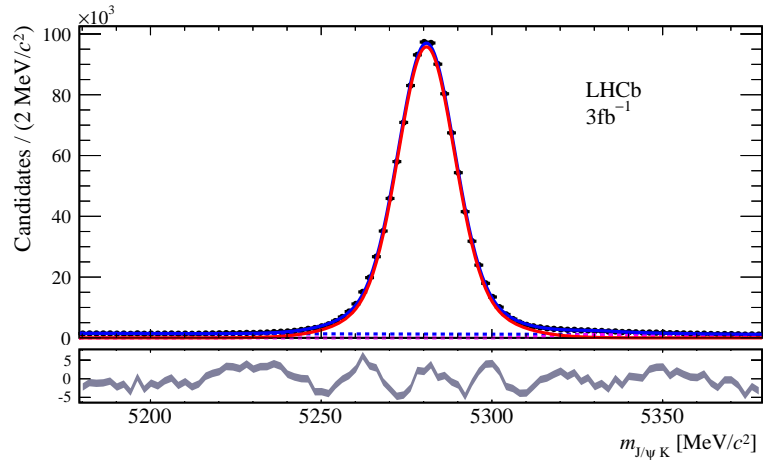

Figure 3: Invariant mass distribution of the $B^+ \to J/\psi K^+$ candidates in data obtained after constraining the J/ψ mass to the PDG value. A fit to the distribution is superimposed (blue continuous line) with signal described with a double Crystal Ball function (red continuous line), combinatorial background described as an exponential function (blue dashed line) and misidentification background from $B^+ \to J/\psi \pi^+$ background (magenta dashed line).

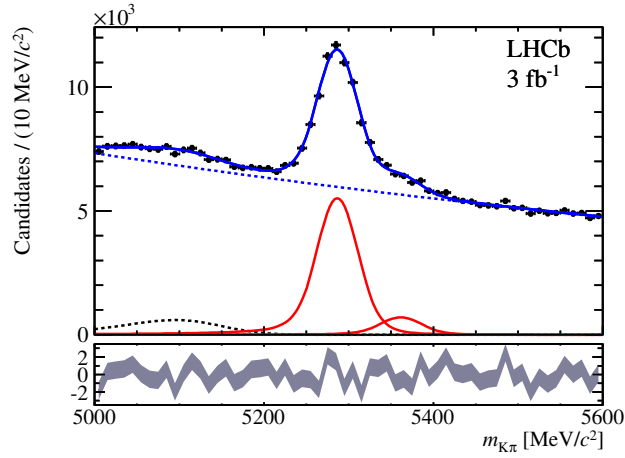Figure 4: Invariant mass distribution of $B^0_{(s)} \to K^\pm \pi^\mp$ candidates in data. A fit to the distribution is superimposed with the signal (red), the combinatorial background (blue dashed), and the partially reconstructed B decay background (black dashed) components shown as well as the full PDF (blue continuous line).
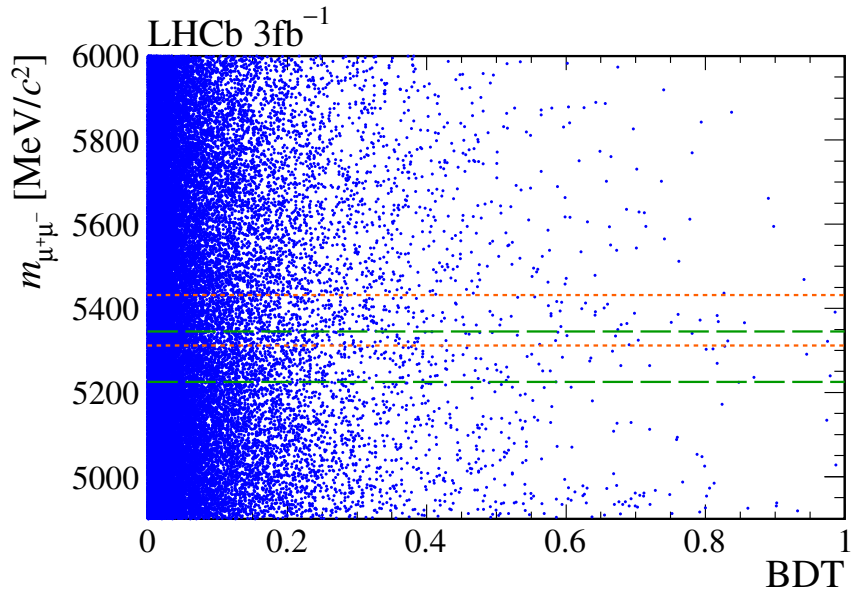

Figure 5: Dimuon mass versus BDT for selected candidates in data. Orange short-dashed (green long-dashed) lines indicate the $\pm 60 \, \mathrm{MeV}/c^2$ search window around the B^0_s (B^0) mass peak values.
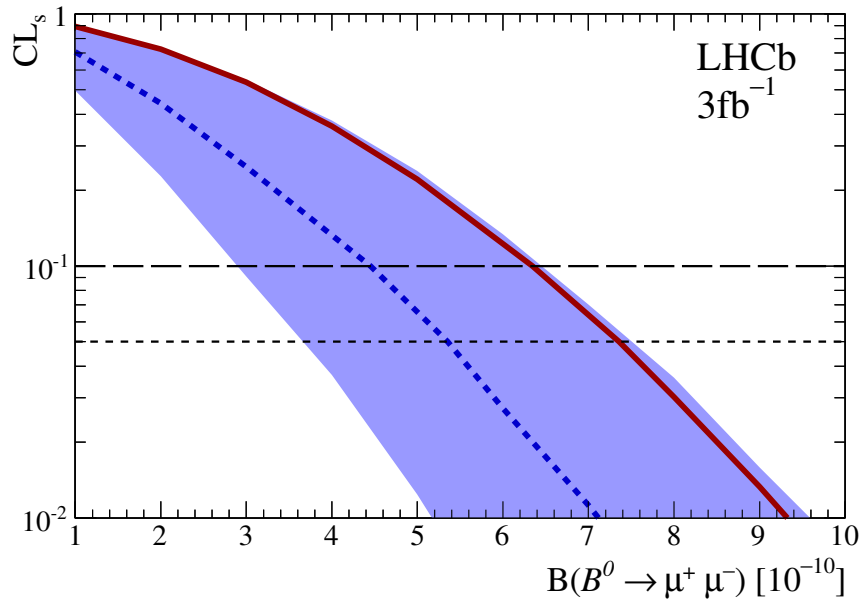
Figure 6: CL$_s$ as a function of the assumed $B^0 \to \mu^+\mu^-$ branching fraction. The dashed curve is the median of the expected CL$_s$ distribution for background and SM signal. The light blue area covers, for each branching fraction value, 34.1% of the expected CL$_s$ distribution on each side of its median. The solid red curve is the observed CL$_s$.
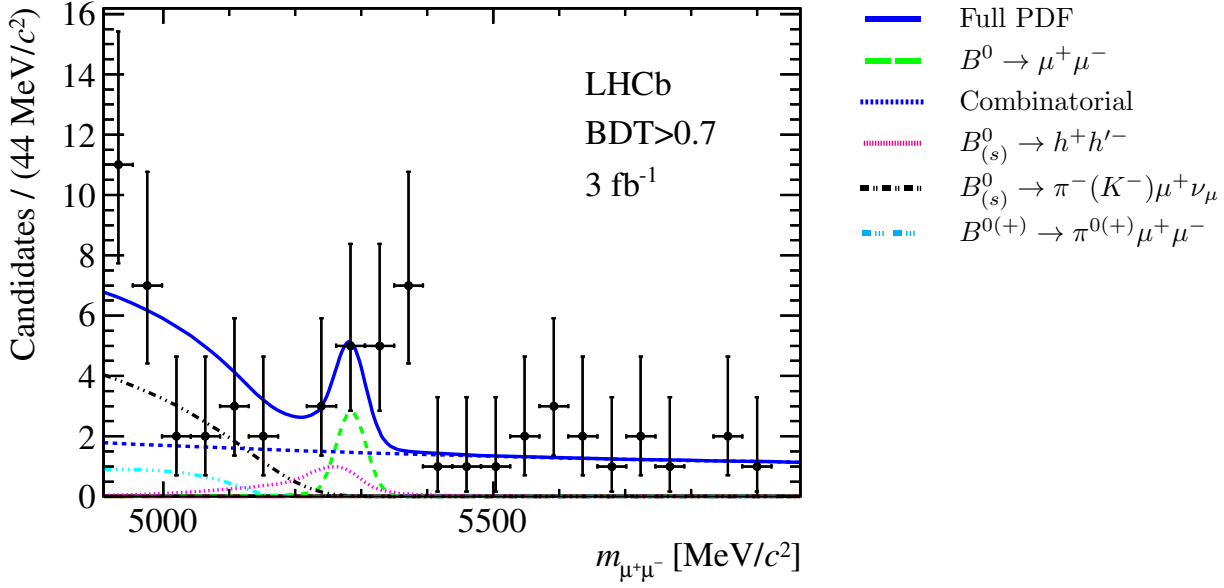
Figure 7: Invariant mass distribution of the selected $B^0_{(s)} \to \mu^+\mu^-$ candidates (black dots) with BDT > 0.7. The projection for BDT > 0.7 of the simultaneous fit to the 8 BDT bins is overlaid (blue solid line). This fit is performed in the background-only hypothesis (no B^0_s signal component fitted) and the different components are: $B^0 \to \mu^+\mu^-$ (green medium dashed), combinatorial background (blue medium dashed), $B^0_{(s)} \to h^+h'^-$ (magenta dotted), $B^{0(+)} \to \pi^{0(+)}\mu^+\mu^-$ (light blue dot-dashed), $B^0 \to \pi^-\mu^+\nu_\mu$ and $B^0_s \to K^-\mu^+\nu_\mu$ (black dot-dashed). [This plot can be used to explain, together with Fig. 2 of the paper, how the significance is computed. This plot illustrate the case of $B^0_s \to \mu^+\mu^-$, thus the $B^0_s \to \mu^+\mu^-$ signal is absent. Note that the $B^0 \to \mu^+\mu^-$ component is present.]
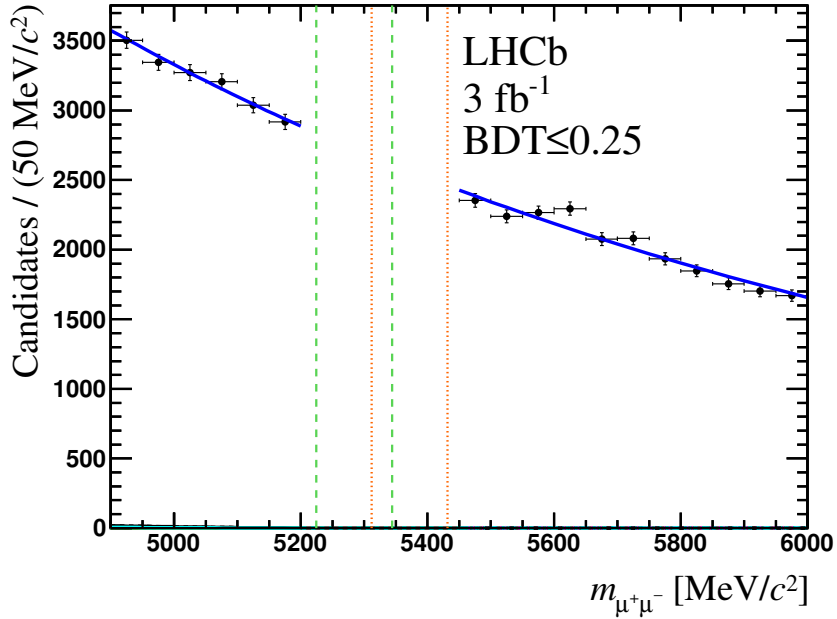
Figure 8: Dimuon invariant mass distribution for $B^0_{(s)} \to \mu^+\mu^-$ candidates in data in the first bin of BDT output. Data is shown prior unblinding of the signal region. A fit to the data points, used to interpolate the background to the signal region, is superimposed. The full PDF (blue line) is represented including an exponential combinatorial background, and background from partially reconstructed $B^0 \to \pi^-\mu^+\nu_\mu$ and $B^0_s \to K^-\mu^+\nu_\mu$ decays (black line), $B^{0(+)} \to \pi^{0(+)}\mu^+\mu^-$ decays (cyan), and misidentified background from $B^0_{(s)} \to h^+h'^-$ decays (green dashed). Vertical orange (green) dashed lines indicate the $B^0_s \to \mu^+\mu^-$ ($B^0 \to \mu^+\mu^-$) search windows excluded from the background estimation fit. [This plot is tipically used to explain how the BDT pdf for bkg (paper Fig. 1) is calibrated on data.]
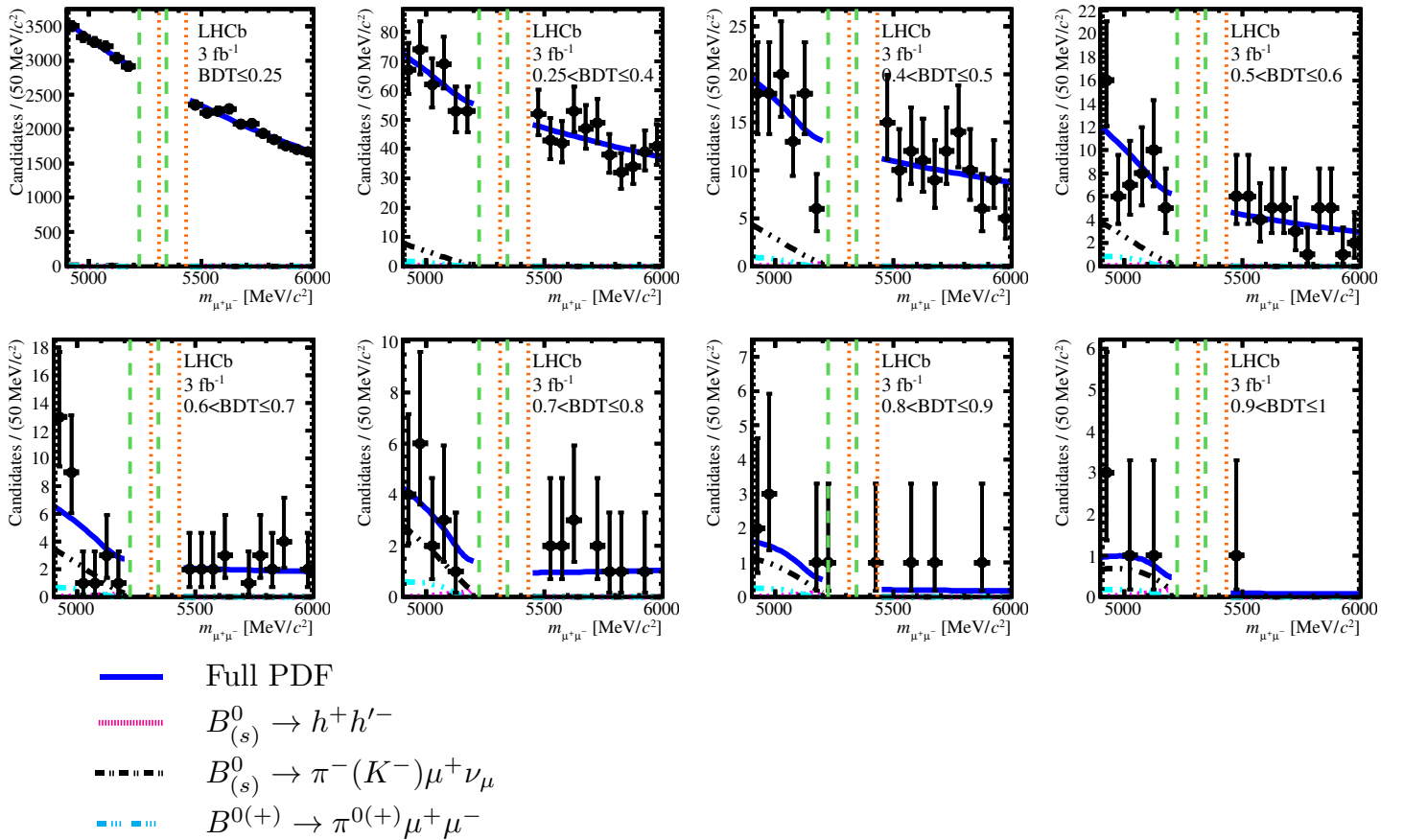
Figure 9: Dimuon invariant mass distribution for $B^0_{(s)} \to \mu^+\mu^-$ candidates in data in 8 bins of BDT output. Data is shown prior unblinding of the signal region. A fit to the data points, used to interpolate the background to the signal region, is superimposed. The full PDF (blue line) is represented including an exponential combinatorial background, and background from partially reconstructed $B^0 \to \pi^-\mu^+\nu_\mu$ and $B^0_s \to K^-\mu^+\nu_\mu$ decays (black line), $B^{0(+)} \to \pi^{0(+)}\mu^+\mu^-$ decays (cyan), and misidentified background from $B^0_{(s)} \to h^+h'^-$ decays (green dashed). Vertical orange (green) dashed lines indicate the $B^0_s \to \mu^+\mu^-$ ($B^0 \to \mu^+\mu^-$) search windows excluded from the background estimation fit.
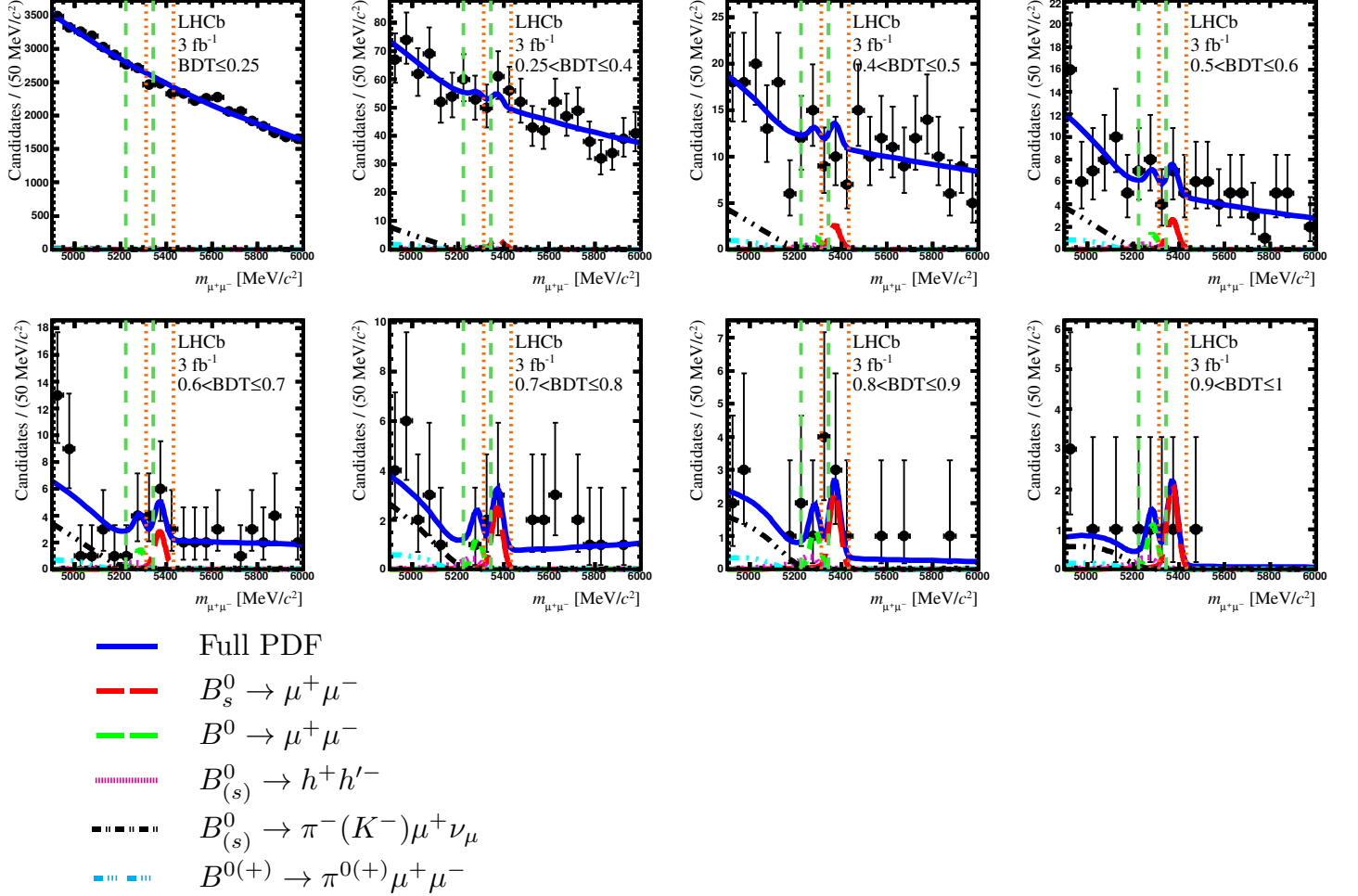
Figure 10: Dimuon invariant mass distribution for $B^0_{(s)} \to \mu^+\mu^-$ candidates in data in 8 bins of BDT output. A fit to the data points is superimposed. The full PDF (blue line) is represented including the $B^0_s \to \mu^+\mu^-$ (red) and $B^0 \to \mu^+\mu^-$ (green dashed) signals, an exponential combinatorial background, and background from partially reconstructed $B^0 \to \pi^-\mu^+\nu_\mu$ and $B^0_s \to K^-\mu^+\nu_\mu$ decays (black dot dahed line), $B^{0(+)} \to \pi^{0(+)}\mu^+\mu^-$ decays (cyan), and misidentified background from $B^0_{(s)} \to h^+h'^-$ decays (green dashed). Vertical orange (green) dashed lines indicate the $B^0_s \to \mu^+\mu^-$ ($B^0 \to \mu^+\mu^-$) search regions.
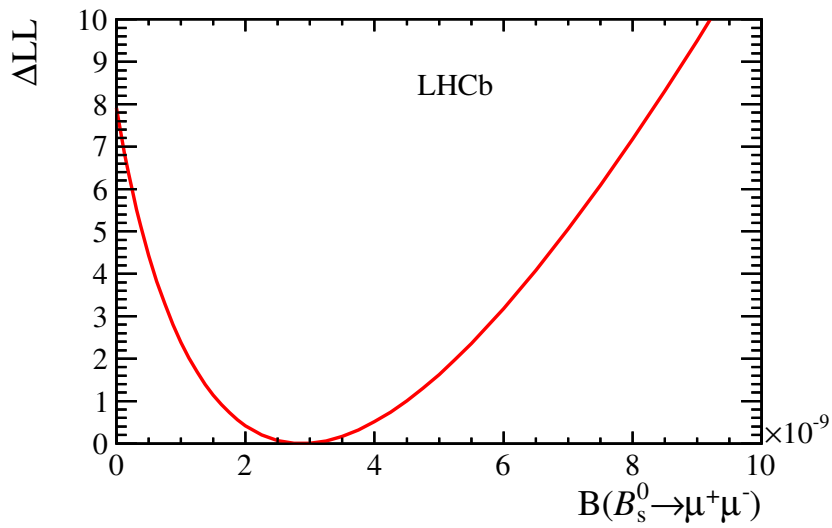
Figure 11: Profile-likelihood ratio scan for the $\mathcal{B}(B_s^0 \to \mu^+\mu^-)$ physics parameter. At each $\mathcal{B}(B_s^0 \to \mu^+\mu^-)$ value in the range scanned, a fit to the data is performed fixing the $\mathcal{B}(B_s^0 \to \mu^+\mu^-)$ (all the other parameters can float as in the best fit). The ratio of the resulting negative log-likelihood to the negative log-likelihood obtained when $\mathcal{B}(B_s^0 \to \mu^+\mu^-)$ can vary (the best fit) is then reported on the graph.
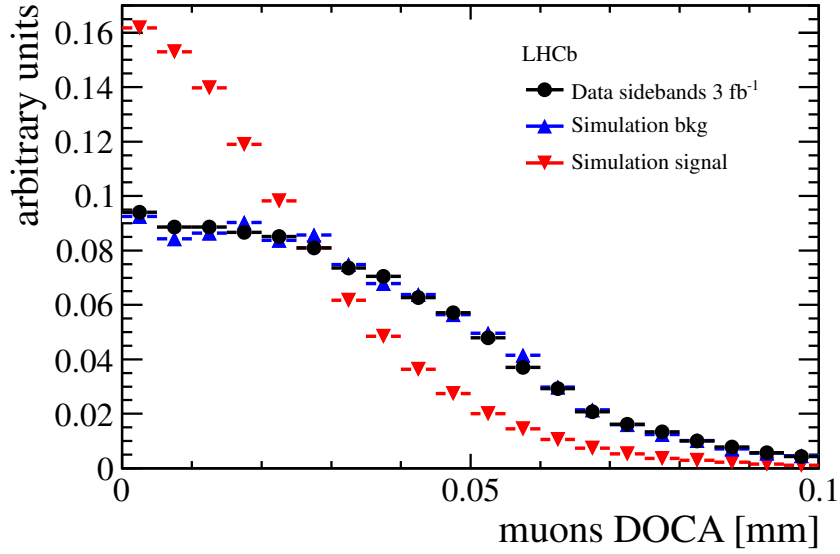
Figure 12: Distribution of the distance of closest approach (DOCA) between the muons of $B^0_{(s)} \to \mu^+\mu^-$ candidates in a simulated sample of signal events (red), in a simulated sample of background events (blue), and in data (black dots)
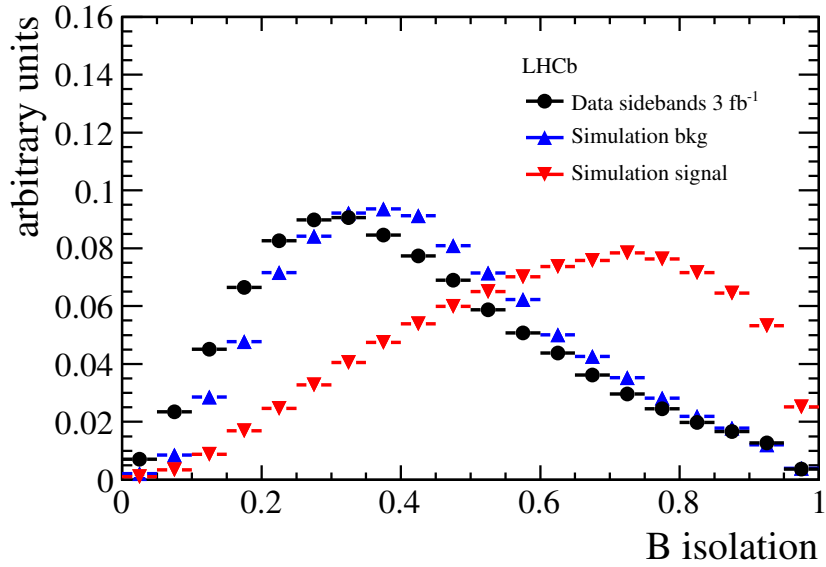

Figure 13: Distribution of the angle between the isolation of the B meson for $B^0_{(s)} \to \mu^+\mu^-$ candidates in a simulated sample of signal events (red), in a simulated sample of background events (blue), and in data (black dots).
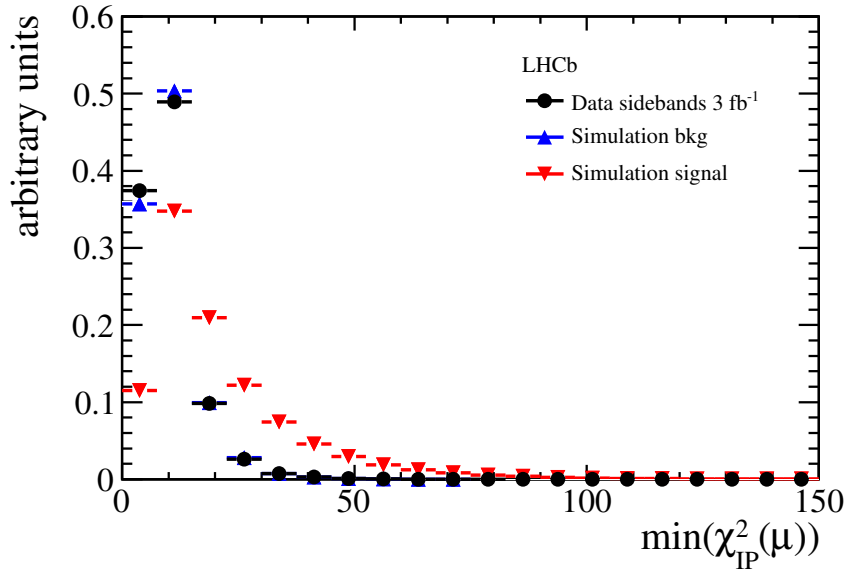
Figure 14: Distribution of the minimum impact parameter significance of the muons of $B^0_{(s)} \to \mu^+\mu^-$ candidates in a simulated sample of signal events (red), in a simulated sample of background events (blue), and in data (black dots).
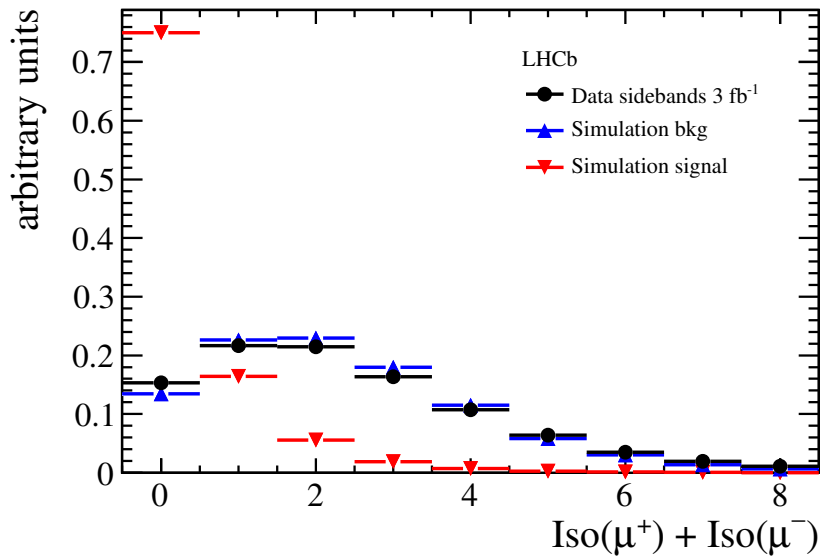

Figure 15: Distribution of the sum of the isolation of the two muons for $B^0_{(s)} \to \mu^+\mu^-$ candidates in a simulated sample of signal events (red), in a simulated sample of background events (blue), and in data (black dots).
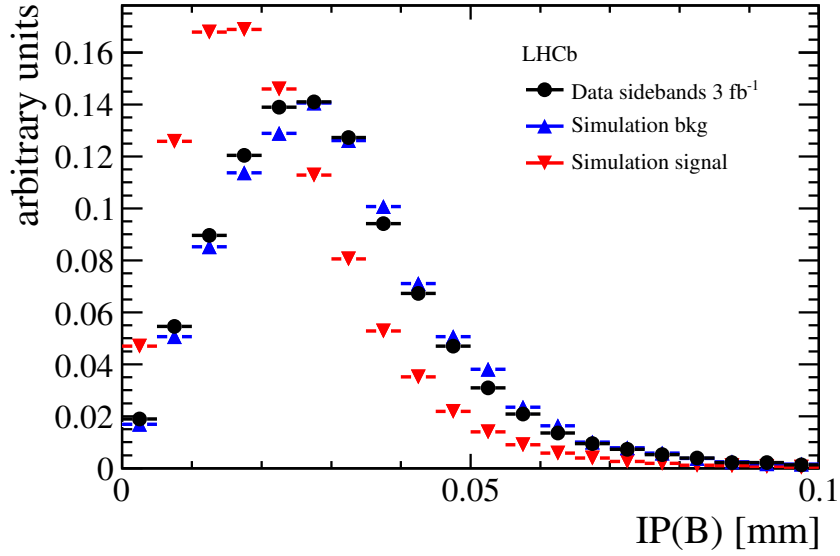
Figure 16: Distribution of the impact parameter of the B meson with respect to the PV for $B^0_{(s)} \to \mu^+\mu^-$ candidates in a simulated sample of signal events (red), in a simulated sample of background events (blue), and in data (black dots).

Figure 17: Distribution of the B meson transverse momentum for $B^0_{(s)} \to \mu^+\mu^-$ candidates in a simulated sample of signal events (red), in a simulated sample of background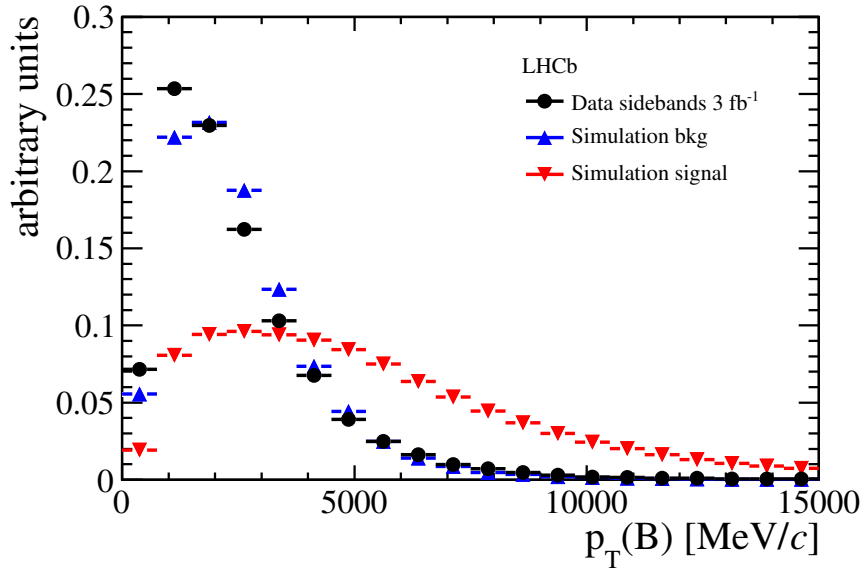 events (blue), and in data (black dots).